DOI: 10.13009/EUCASS2022-6128

Effect of electron number densities on the radio signal attenuation in an inductively coupled plasma facility

Diana Luís[a,b†], Alan Viladegut[a], Adriano Camps[b] and Olivier Chazot[a]
[a]*von Karman Institute for Fluid Dynamics, Chaussée de Waterloo 72, 1640 Rhode-Saint-Genèse, Belgium*
[b]*Universitat Politècnica de Catalunya, UPC-BarcelonaTech, Barcelona 08034, Spain*
diana.luis@vki.ac.be · alan.viladegut@vki.ac.be · adriano.jose.camps@upc.edu · chazot@vki.ac.be
†Corresponding author

Abstract

Spacecraft entering a planetary atmosphere are surrounded by a plasma layer containing high levels of ionization. The high electron number densities cause attenuation of the electromagnetic waves emitted by the on-board antennas, leading to communication blackout for several minutes. This work presents experimental measurements of signal propagation in an ionized plasma flow. These measurements are conducted at the VKI plasma wind tunnel using conical horn antennas transmitting in the Ka-band, between 33 and 40 GHz. Clear attenuations are observed when the signal is propagating through the plasma. These vary between 5 and 15 dB depending on the testing conditions. Preliminary evidence of Faraday rotation effect caused by the plasma is also observed. Additionally, high speed imaging analysis shows significant jet fluctuations, related with the chamber pressures and power settings.

1. Introduction

Spacecraft enter planetary atmospheres at hypersonic velocities generating shock waves ahead of the vehicle and consequent extreme aerodynamic heating. The high post-shock temperatures dissociate and ionize the gas creating a plasma layer that surrounds the spacecraft. High ionization degrees affect the propagation of the electromagnetic waves emitted by the on-board antennas, causing attenuation and refraction of the radio waves. Extreme ionization levels lead, ultimately, to a communication blackout. Figure 1 shows a schematic representation of this phenomenon. The radio communication blackout occurs when the characteristic frequency of the plasma layer around the vehicle exceeds the radio frequency used for communications. The ionization degree of the gas defines the plasma frequency, f_p [Hz], which is related to the electron number density, n_e [m^{-3}], by

$$f_p = \frac{1}{2\pi}\sqrt{\frac{q_e^2 n_e}{m_e \epsilon_0}} \approx 9\sqrt{n_e} \tag{1}$$

where q_e and m_e are, respectively, the electron charge and mass, and ϵ_0 the free space permittivity. Radio blackout typically lasts several minutes, depending on the trajectory and altitude of the vehicle, the properties of the atmosphere[1] and the frequency of the emitting antenna. The attenuation rate of the signal κ [dB m^{-1}] is given by[2]

$$\kappa = \frac{54.6}{\lambda}\sqrt{\frac{f_p^2 - f^2}{f^2}}, \tag{2}$$

where λ and f are the wavelength and frequency of the electromagnetic wave being used for communication. Attenuation rates for various commonly used communication bands (calculated using Eq. 2) as a function of the electron number density are plotted in Fig. 2. Peak plasma densities encountered in historic missions[3–6] are plotted on vertical lines. Figure 2 motivates that the key to the solution of the reentry blackout problem lies in a reduction of the electron densities in the plasma layer.

From the beginning of space exploration, different methodologies for actively reducing the plasma layer effects on radio communication attenuation and blackout have been proposed and studied. The most promising areas of research are high-frequency transmission, creation of a magnetic field, aerodynamic shaping effects,[7] electrophilic injection,[8] and Raman scattering.[9] During the 1960s, NASA's radio attenuation measurement program[10] was conducted

DOI: 10.13009/EUCASS2022-6128

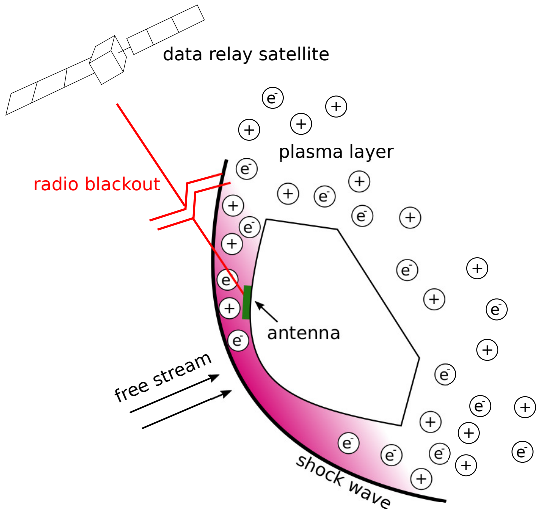

Figure 1: Schematic of the blackout phenomenon during reentry.

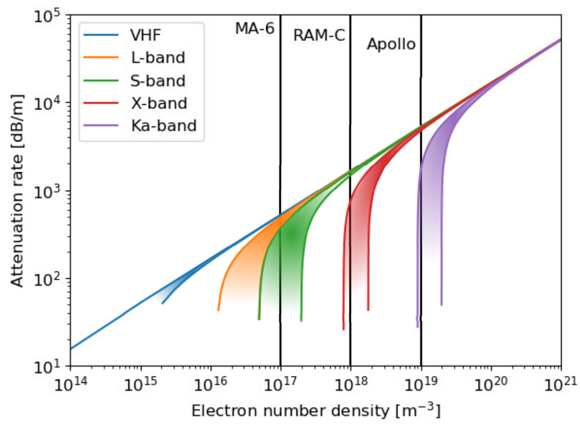

Figure 2: Attenuation rates for various typical frequency bands used in space communications and peak plasma densities encountered in the antenna regions of the MA-6, RAM-C and Apollo missions.[3–6]

to develop diagnostics for characterization of reentry plasma parameters and to begin in-flight testing of some mitigation methods. Those studies confirmed that the most feasible methods mainly contained electrophilic injection, and magnetic windows.[11] However, no method has been successfully integrated into a spacecraft for regular flight.

In ground facilities, several experimental campaigns have been performed. Significant success at mitigating the blackout conditions have been observed using a remote antenna assembly (RAA) in hypersonic wind tunnels for different Mach numbers.[12] A RAA is a small antenna assembly mounted on a pylon in the nose of the fuselage and placed ahead of the bow shock of the vehicle, i.e., outside the thick shock layer. This study showed that acceptable ionization levels near the antennas can be achieved to allow communications. However, the RAA usually melted without the use of an active cooling system.[13] Savino et al.[14] conducted an experimental campaign in an arc jet plasma wind tunnel to reproduce the plasma frequency on ground and to numerically correlate it with the radio frequency signal loss. For that, they conducted a preliminary characterization of the plasma density and electron temperature using a Langmuir probe. This study demonstrated the capability of duplicating the ionization levels encountered during reentry, and the ability of arc jet facilities, integrated with proper numerical tools, to correctly deal with problems of communication attenuation and blackout. Bendoukha et al.[15] explored a new method of communication called end of radio silence using an arc heat facility. A transmitter was located behind the thermal shield, and the receiver equipped with wire antenna was installed in the vacuum chamber and outside the hot gas flow to receive radio signal during the transmissions. However, the main purpose of the research was to test the performance of the heat shield while protecting the antenna. Lemmer et al.[16] performed experiments to evaluate the use of crossed electric and magnetic filed to lower the plasma density in a region surrounding the antenna. These measurements were conducted in a 150-mm diameter helicon plasma source operating with argon. The electron number densities, plasma frequency and signal attenuation measurements were done with a Langmuir probe, a hairpin resonance probe and a S2-1 probe, respectively. They found this approach to be a feasible method for communication blackout amelioration and the plasma number density to decrease up to 70%. The attenuation levels improved from -10 dB to -2 dB for frequencies in the L-band. Schlachter et al.[17] developed a conduction cooled High Temperature Superconducting (HTS) magnet to provide a high magnetic field for a radio blackout mitigation experiment in DLR L2K arc heated wind tunnel. Their experiments also used the $E \times B$ communication blackout scheme to reduce locally the electron density of the argon plasma. Their experimental setup used a flat plate model with a transmitter antenna and a superconducting magnet, positioned in a region with lower plasma number density to avoid attenuation and reflections of the radio waves.

The Horizon 2020 MEESST (Magnetohydrodynamic Enhanced Entry System for Space Transportation) project aims at designing and testing a proof-of-concept magnetic shielding device for mitigation of radio blackout and for reduction of heat flux upon the surface of the spacecraft during atmospheric entry. The interaction between the magnetic field lines and the electrons prevents the electrons to respond to the electric field component of the electromagnetic oscillation from radio communications.[18] This effectively creates a magnetic window through which communication signals can freely pass. Analytical work[19,20] showed that the magnetic field required to allow the communication frequencies to penetrate the reentry plasma must be very strong. These strong magnetic fields are conceivable to generate forces which can modify the fluid dynamics configuration, such as moving the shock front away from the vehicle surface which decreases the thermal flux towards the wall and the electron number densities.

DOI: 10.13009/EUCASS2022-6128

As part of the project, this work presents the effects of an ionized medium on the propagation of the radio signal through an air plasma flow produced with the Inductively Coupled Plasma (ICP) generator in the VKI-Plasmatron facility. As a first attempt to characterize the radio wave propagation through the plasma, two antennas are placed aligned perpendicularly to the plasma flow, and the attenuation of the signal is assessed. Additionally, the instabilities of the plasma flow are also studied due to their influences to the signal propagation.

2. Radio communication theory

2.1 Signal propagation in ionized mediums

The characteristics of electromagnetic wave propagation in the atmosphere depend strongly on the operating frequency. The ionosphere has a major effect on the propagation at medium and high frequencies (0.3-30 MHz), because radio waves in this frequency range are effectively reflected. For frequencies above 30 MHz, the waves propagate through the atmosphere with small attenuation, allowing satellite and deep space communications. At frequencies above 10 GHz, atmospheric conditions play a major role in the signal propagation.[21]

The ionosphere is a region of highly charged particles that form an ionized gas or plasma. As such, the ionospheric propagation theory can be extended to plasma flow on ground facilities. The "reflections" from the ionosphere are produced by refraction as the wave propagates through this region. The relative dielectric constant of the plasma[22] is

$$\epsilon_r = 1 - \frac{f_p^2}{f^2(1 - j\nu/(2\pi f))}, \tag{3}$$

where f_p is the plasma frequency defined in Eq. 1, f the antenna frequency, and ν is the electron collision frequency. Neglecting the collisions,

$$\epsilon_r = 1 - \frac{f_p^2}{f^2}. \tag{4}$$

The propagation constant of a wave in a plasma[23] corresponding to the imposed frequency f is

$$k = k_0 \sqrt{1 - \frac{f_p^2}{f^2}} = k_0 \sqrt{\epsilon_r}. \tag{5}$$

Hence, for frequencies $f > f_p$, the propagation constant is real and the wave is refracted by the plasma according to the variation of ϵ_r. For frequencies $f < f_p$, the dielectric constant is negative, which leads to an imaginary propagation constant. In this case, an incident wave on the medium is totally reflected. Additionally, for frequencies $f \gg f_p$ the relative dielectric constant is essentially one, and the wave passes through the plasma without significant refraction. However, if the plasma is magnetized, the waves undergo Faraday rotation by the ionized medium, and the polarization vector is rotated as the wave passes through it.

The total electron content (TEC) accumulated along a transmission path penetrating the ionosphere causes the rotation of the wave polarization (Faraday rotation), time delay of the signal, and a change in the apparent direction of the arriving signal due to refraction. As the rotations and time delays are non-linearly dependent of the frequency, a dispersion or group velocity distortion can also occur. The magnitude of the Faraday rotation, θ [rad], depends on the frequency of the radio wave, the magnetic field strength, and the electron density of the plasma as

$$\theta = 2.36 \times 10^4 \frac{B_{av} N_T}{f^2}, \tag{6}$$

where θ is the angle of rotation, B the average Earth magnetic field, f the frequency, and N_T the TEC [m^{-2}] expressed as

$$N_T = \int_S n_e(s) ds, \tag{7}$$

being s is the propagation path and n_e the electron number density.

The presence of charged particles in the ionized medium also slows down the propagation of the radio signal along the path. This time delay in excess of the propagation time in free space is called the group delay, t [s], and it is computed as

$$t = 1.345 \times 10^{-7} \frac{N_T}{f^2}. \tag{8}$$

Figures 3a and 3b presents, respectively, the evolution of the Faraday rotation for an average value of the Earth's magnetic field strength of 50 μT and of the group delay, for different TEC values in the Ka-band (26 to 40 GHz).

DOI: 10.13009/EUCASS2022-6128

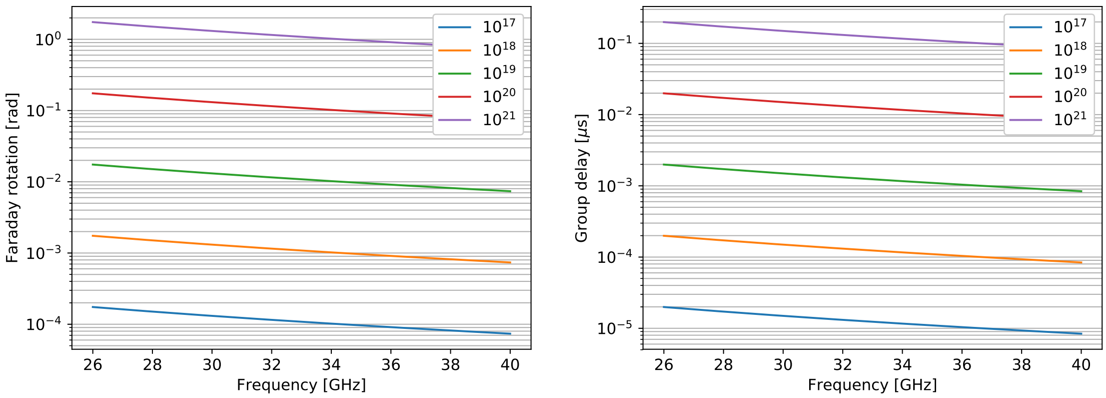

(a) Faraday rotation for $B_{av} = 50\ \mu$T. (b) Group delay.

Figure 3: Effects due to electron concentration function of TEC and frequency in the Ka-band.

2.2 S-parameters

For high frequencies, a network is represented by its scattering matrix. This S-matrix allows to describe the properties of a multi-port network by quantifying how electromagnetic energy propagates through the network. The scattering term refers to the relationship between incident and scattered (reflected and transmitted) travelling waves. The S-matrix for a N-port network contains N^2 complex coefficients (S-parameters), each one representing the magnitude and phase of a possible input-output path. The diagonal parameters are referred to as *reflection* coefficient and the off-diagonal parameters as *transmission* coefficients.

The waves going through the N-port are $\mathbf{a} = (a_1, a_2, ..., a_N)$ and the waves travelling away are $\mathbf{b} = (b_1, b_2, ..., b_N)$. The wave a_i going into port i is derived from the voltage wave going into a matched load. For consistency with the conversation of energy, the voltage is normalized to $\sqrt{Z_0}$, being Z_0 the characteristic impedance (often $Z_0 = 50\Omega$). The definitions of the waves a_i and b_i are

$$a_i = \frac{V^+}{\sqrt{Z_0}}, \quad b_i = \frac{V^-}{\sqrt{Z_0}} \tag{9}$$

where V^+ is the voltage of the incident wave and V^- the voltage of the reflected wave. The relation between a_i and b_i ($i \in 1, 2, ..., N$) can be written as a system of N linear equations[24]

$$b_i = S_{ii}a_i + S_{ij}a_j, \tag{10}$$

where the j subscript stands for the port that is excited (the input port), and the i subscript for the output port. Physically, S_{ii} is the input reflection coefficient with the output of the network terminated by a matched load ($a_j = 0$); S_{ij} is the transmission from port j to port i; and S_{jj} the output reflection coefficient. Figure 4 represents a generalized two-port network with a characteristic impedance of Z_0.

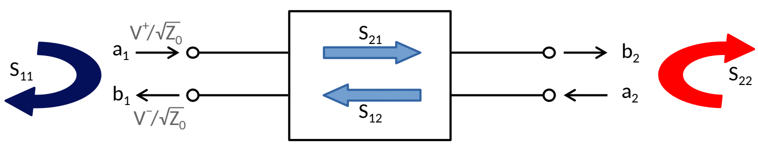

Figure 4: Generalized two port network.

3. Experimental setup

3.1 The Plasmatron facility

The Plasmatron at the von Karman Institute for Fluid Dynamics (VKI) is an inductively-coupled plasma (ICP) wind tunnel,[25] that creates a high enthalpy, highly dissociated subsonic gas flow for reproduction of the aerothermodynamic environment found in hypersonic flight regimes. This facility has been extensively studied by Bottin et al.[25,26]

DOI: 10.13009/EUCASS2022-6128

Its basic concept consists of a quartz tube with an internal diameter of 200 mm and 5 mm thickness surrounded by a coil, which is connected to a 1.2 MW generator that provides high voltage (2 kV) and high frequency (400 kHz) current. This induces an electromagnetic (EM) field inside the tube, that forces residual charged particles in the flow to form eddy currents which heats up the gas by Joule effect. The injection of gas is done through a ring-shaped inlet at the outer edge of the torch. Due to the induced EM field, the gas ionizes into plasma flow, which exits at subsonic speed into a low pressure test chamber. Argon is employed as starting gas, facilitating the initial electric discharge, due to the longer lifetime of the free electrons at low pressure compared to the air plasma case. Then, the gas is gradually switched to the desired test gas (air, N_2, CO_2) and the argon switched off. The plasma exits through a diffuser, and it is cooled down by a water cooled heat exchanger. The vacuum system consists of a set of three pumps. After proper dilution, the recombined gases are finally released to the atmosphere through an exhaust. Complementary systems are responsible for the gas circulation, cooling, and diagnostics.

An absolute pressure transducer (Memberanovac DM 12, Leybold Vacuum) measures the static pressure (p_s) in the test chamber. As the plasma jet is low subsonic (Ma $\approx$ 0.1), the static pressure is assumed constant inside the chamber. The gas mass flow rate ($\dot{m}_{gas}$) supplied to the torch is monitored through a calibrated gas rotameter (Bronkhorst EL-Flow F-203AV), while the Plasmatron control system allows to record the electric power (P_{el}) supplied to the induction coil. Suitable side windows provide the necessary optical access to the testing chamber perpendicular to the plasma flow.

3.2 Experimental setup design

A preliminary numerical analysis is performed to estimate the plasma frequency and, consequently, to design the appropriate communication system. The subsonic steady state plasma flow field in the Plasmatron chamber is numerically simulated using the in-house ICP magnetohydrodynamics solver.[27,28] This solver couples the Maxwell equations with the Navier-Stokes equations under Local Thermodynamic Equilibrium (LTE) and axisymmetric steady flow assumptions. The VKI ICP code is integrated into the Computational Object-Oriented Library for Fluid Dynamics (COOLFluiD).[29] This solver simulates the interaction between the electromagnetic field around the coil and the gas passing through, with the aim of reproducing the whole Plasmatron chamber. The ICP computations use the VKI-developed Mutation++[30] library to determine thermodynamic and transport properties of the 11-species air mixture, including O_2, N_2, O_2^+, N_2^+, NO, NO^+, O, O^+, N^+, N and e^-. In the simulations, all the walls are cooled down to 350 K and the annular injection of the gas is imposed at the inlet.[31] The input parameters are the static pressure in the Plasmatron chamber, the gas mass flow rate supplied to the torch, and the effective power dissipated in the plasma by electromagnetic induction. The static pressure and mass flow rate are experimentally measured during the test with the absolute pressure transducer and the gas rotameter, respectively. The exact value for the effective power generating the plasma is unknown and generally an efficiency of 50% of the electric power is considered.

The following analysis considers a database of simulations at a constant mass flux of 16 g/s, static pressures of 15, 50 and 100 mbar, and varied effective powers, under LTE assumption. Three different positions along the center of the axis are analysed (18.4, 31.5 and 44 cm from the torch exit). Figure 5 summarizes the evolution of the numerical electron number densities with static pressure and effective power, and communication bands between 8 GHz (7.9×10^{17} m^{-3}) and 110 GHz (1.5×10^{20} m^{-3}). The simulations show that the further away from the torch exit, the lower the electron densities, with more significant differences at intermediate powers. Based on these results, the Ka-band is chosen. This bandwidth allows to study testing conditions where the signal can propagate through the plasma (if $f_p < f$) and conditions in complete blackout (if $f_p > f$). Additionally, the range of electron number densities in this band simulates flight conditions of Apollo missions (as shown in Fig. 2).

3.3 Experimental setup and calibration

From the previous analysis, the communication system is defined in the Ka-band. The setup is composed of two sets each comprising a conical horn antenna with circular waveguide, linear polarization and 15 dBi gain (MI-wave 262A-15/0.250), a mode transition (MI-wave 284-0.250) and a waveguide to coax adapter (MI-wave 411A). Each of these sets is connected to, respectively, a 3 m and a 3.5 m flexible microwave cable (Huber-Suhner SUCOFLEX 102) and a DC block (MI-wave 8141A). The transmission and reception of the signal are performed with a vector network analyser (VNA, Rohde and Schwarz ZNB40). Details about these parts are summarized in Table 1. The combination of these instruments allow operating between 33 and 40 GHz. As such, the sweep frequency of the VNA is defined between 33 and 40 GHz, with 201 default points in between these limits, and a frequency step size of 60 MHz. The VNA operates with a sweep time of 43.617 ms and a sampling frequency of 4.6 kHz.

From the gains and losses in the system, a link budget can be estimated. The radio link budget sums the transmitted power along with the gains and losses of every subsystem to determine the signal strength arriving at the receiver

DOI: 10.13009/EUCASS2022-6128

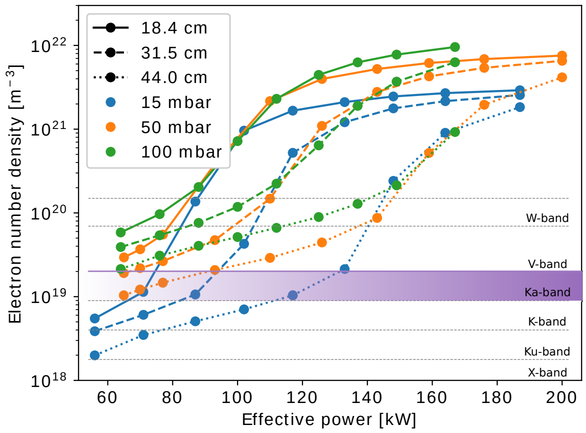

Figure 5: Evolution of the numerical electron number densities along the axis of the jet.

Table 1: Details about the instruments.

Instruments	Antenna	Mode transition	Adaptor	Cable 3 m / 3.5 m	DC block	VNA
Connectors	custom flange	custom flange	custom flange - 2.92 mm (f)	2.92 mm (m - f)	2.92 mm (m - f)	2.92 mm (m)
Operating frequency [GHz]	33 - 38.5	33 - 38.5	26.5 - 40	up to 46	0.01 - 40	0.01 - 40
Link budget	15 dBi	0 dB	- 0 .4 dB	- 7.87 dB / - 9.18 dB	- 0.75 dB	10 dBm

input. For this case, the link budget equation for the radio communication system is

$$P_R = P_T + G_T - L_T - L_{FP} + G_R - L_R, \tag{11}$$

where P_R is the received power in dBm, P_T the transmitter output power from the VNA [dBm], G_T and G_R are, respectively, the transmitter and receiver antenna gains [dBi], L_T and L_R the losses [dB] associated to transmitter and receiver adaptors, cables and DC blocks, and L_{FS} the free space loss [dB]. The latter loss can be estimated as

$$L_{FS} = 20\log_{10}\left(\frac{4\pi d f}{c}\right) \tag{12}$$

where d is the distance between the antennas, f the operating frequency, and c the speed of light. For this experimental campaign the antennas are positioned 2 m from each other outside of the side windows of the Plasmatron. Even though the windows also introduce losses, these are neglected here due to lack of data. For an operating frequency of 40 GHz, the link budget provides a received power of -49.1 dBm. The dynamic range of the VNA is 120 dB, so meaningful measurements are still expected to be achieved.

The systematic calibration of the system is performed using a 2.92 mm network analyzer calibration kit (Rohde and Schwarz ZN-Z229). This type of calibration ensures that the effects of cables and DC blocks, and all systematic errors in general are canceled out before the measurements of the radio signal of the antennas. For this work, TOSM (thru-open-short-match) full 2-port calibrations are performed. The full 2-port calibration ensures that all four S-parameters are fully corrected. TOSM is a defined standards calibration, requiring that data describing all of the reflection standards (provided by the factory) is loaded into the VNA on a serial number basis. As the behaviour of the standards are known, measuring them with a VNA defines all of the error terms.[32] The load behaviour sets the directivity terms, the short and open circuits determines the source match and reflection tracking, and the thru determines the transmission tracking and load match.

High speed camera (HSC) imaging is also performed using a complementary metal-oxide-semiconductor (CMOS) camera (SpeedSense M310, Vision Research). The camera is characterized by a depth of 12 bit and by a black and white sensor. The HSC is equipped with a 24 mm focal length objective to ensure the complete visualization of the plasma flow field. The image resolution is set for 1024 × 768 pixels, and the acquisition rate to 4.1 kHz. The sample rate, exposure time, and exposure rate are changed according to the testing power as summarized in Table 2. To synchronize the recording of the VNA and of the HSC, a pulse generator (DG535, Stanford Research Systems) is used to send a trigger pulse for both instruments simultaneously. A schematic of the complete setup is represented in Fig. 6. The acquisition period of the HSC after trigger is set to 49 ms, with a total number of 201 acquired frames.

DOI: 10.13009/EUCASS2022-6128

Table 2: Summary of HSC conditions.

Power [kW]	Sample rate [fps]	Exposure time [μs]	Exposure index
90	4100	240	64000
100	4100	240	64000
200	4100	100	20000
320	4100	20	20000
400	4100	10	20000
500	4100	3	20000
600	4100	3	20000

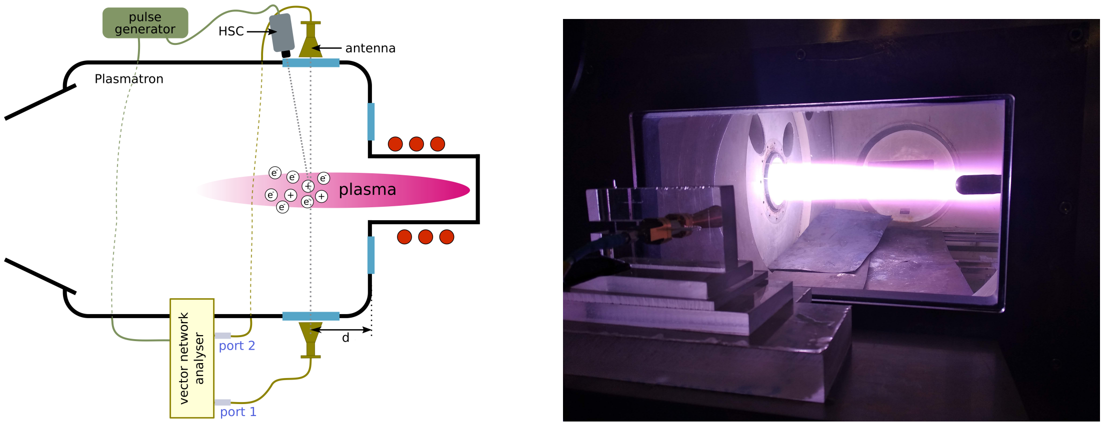

(a) Schematic comprising the antenna sets, VNA, HSC and pulse generator.

(b) Photo taken during a test with one of the antennas visible.

Figure 6: Experimental setup.

4. Results and discussion

4.1 Test conditions

To study the signal propagation in ionized mediums and to try to correlate them with the amount of electrons in the flow, several conditions are tested. These conditions allow gathering data in the operating envelope of the Plasmatron. A summary of the testing conditions is presented in Table 3. Three distinct pressures and two different distances between the antennas and exit of the torch (d) are tested, for increasing electric powers. For each day of experiments, a new calibration and alignment are done. The alignment is done using a 360^o self-leveling laser (Makita SK700D), by aligning it with the center of the torch exit (and center of the windows) and with the center of the antennas in a perpendicular direction, for a certain distance d from the torch exit.

Table 3: Summary of testing conditions.

Distance (d) [cm]	Gas mixture	Mass flow [g/s]	Static pressure [mbar]	Electric power [kW]	HSC
40	air	16	15	90, 100, 200, 320, 400	no
40	air	16	50	90, 100, 200, 320, 400, 500, 600	no
40	air	16	100	200, 320	no
31	air	16	15	90, 100, 200, 320, 400	yes
31	air	16	50	90, 100, 200, 320, 400, 500, 600	yes
31	air	16	100	200, 320, 400, 500, 600	yes

For each of the targeted pressures, three measurements without plasma are taken. The average of these signals for each frequency is considered as background signal. This signal allows to neglect the influence of the quartz windows

DOI: 10.13009/EUCASS2022-6128

and intrinsic reflections on the metallic walls of the chamber. To proceed with the experiments, the Plasmatron is switched on and the air mass flow is set to 16 g/s with the calibrated rotameter. The vacuum pumps are then regulated until the target static pressure is reached inside the chamber. Once the required conditions are reached, five random samples are taken. The static pressure uncertainty can be considered to be ±10% due to the stability of the vacuum pumps.[31,33]

4.2 Experimental results

4.2.1 Plasma instabilities

The investigation of the visible light emission at high acquisition rates using the high speed camera allows to get a qualitative picture of the unsteadiness occurring in the freestream region of the plasma. Figure 7 illustrates frames of the flow at 50 mbar for 100, 200 and 400 kW during 7.6 ms (every five frames taken). As the setting of the HSC are adapted depending on the lighting of the flow at each testing condition (see Table 2), the intensity is normalized for each case. Although low speed cameras and naked eye observations resemble temporally stable flows, high speed imaging reveals significant fluctuations. These fluctuations are clearly dependent on the power (see Fig. 7) but also on the static pressure.

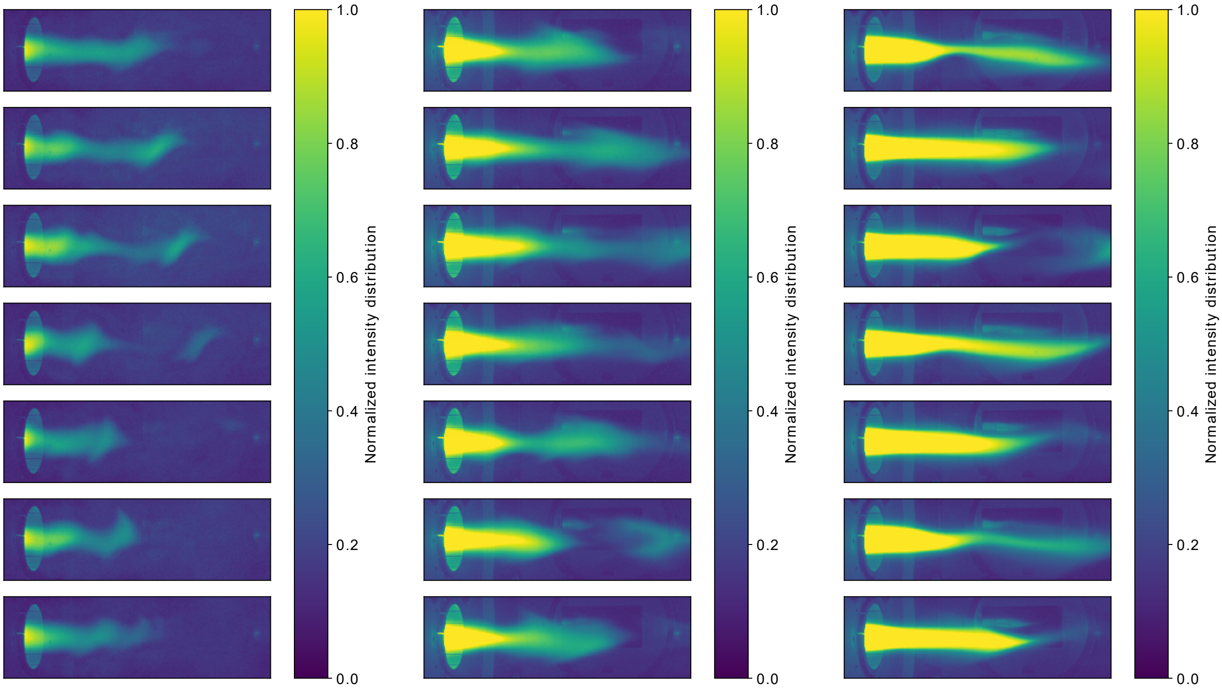

(a) 100 kW (b) 200 kW (c) 400 kW

Figure 7: Evolution of the plasma state for 50 mbar during 7.6 ms.

The highest light emission is located along the axis and close to the exit of the torch. The further away from the torch, the more unstable the plasma jet fluctuates. Correlating higher intensities with higher temperatures and higher electron densities, the intensity of the radio signal passing through the flow should vary accordingly to the fluctuating frequency of the plasma. This is, the attenuation of the transmission signal should be higher for brightest flows. However, according to the manufacturer specification, the antenna has a 23^o at 3 dB beam width E-plane. At the center of the jet, this corresponds to an integration length for each side of the antenna of 20.3 cm. (which is about 2.7 times the diameter of the torch exit). Thus, at a certain instant, the signal encounters different electron densities. Moreover, at the other side of the propagation path, the integration length at 3 dB beam width is 40.6 cm. This implies that the signal reaches the wall of the torch and that multiple reflections occur. As previously mentioned, this effect is dumped in the following signal propagation measurements by subtracting the background signal.

To investigate the frequency components of the emitted light, fast Fourier transform (FFT) is applied to the point of intersection between the line of sight of the antennas and the streamline at the torch centerline. This analysis provides information about the frequency components of the fluctuations of the plasma jet. Figure 8 presents the FFT magnitudes of the light fluctuations at 50 mbar for powers between 100 and 600 kW (for three samples at each

DOI: 10.13009/EUCASS2022-6128

condition). This analysis shows that there is a clear main frequency component that increases with the increase of the power. No other significant components are visible in the spectrum, except occasionally an harmonic or at 600 Hz. This latter frequency corresponds to the frequency of the rectifier that is 12 times the network frequency.[34]

The main frequency component as a function of the power is presented in Fig. 9, for the tested pressures. The error bars correspond to the standard deviation when comparing the samples taken at a certain testing condition. It is observed that the peak shift observed in Fig. 8 is repeated for the other pressures. This yields a clear correlation between the plasma jet fluctuations with the chamber pressure, and power settings of the Plasmatron. Cipullo et at.[34] associated the overall unsteadiness behaviour of the jet to being proportional to the axis velocity at the torch exit. The only exception is observed at 15 mbar and 600 kW (grey point). However, the frequency analysis is restricted at 2060 Hz (due to the HSC acquisition time recorded), which is already close to the frequency for 500 kW. Therefore, further tests should be conducted at 15 mbar and 600 kW with a longer test time to verify if the main frequency indeed decreases or if there is a constraint due to the time interval recorded.

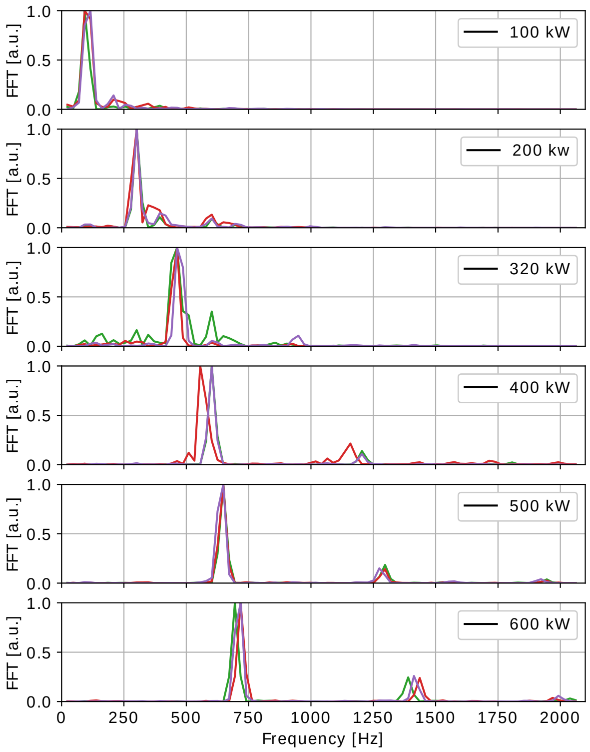

Figure 8: FFT of the light emission fluctuations at 50 mbar.

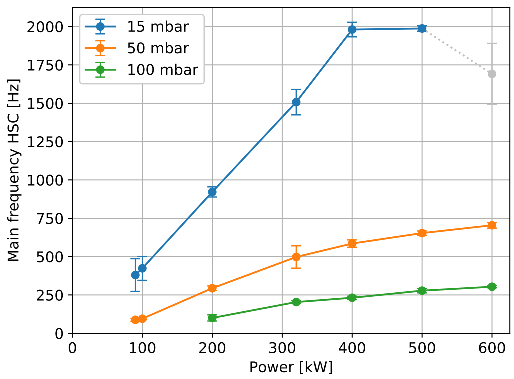

Figure 9: Main frequency component of the plasma jet.

4.2.2 Influence of the windows without plasma

Preliminary tests are conducted without plasma to study the influence of the metallic walls and of the quartz windows on the propagation of the signal. The antennas are placed outside of the windows, 40 cm from the torch exit, and the distance between them is kept as constant as possible, at around 2 meters. Figure 10 presents the magnitude of the S parameters when the windows are opened (blue lines) and closed (orange lines). The increase in magnitude of the S11 and S22 parameters when introducing the windows indicates an increase of the reflected signal from each of the antennas. The lack of reciprocity between the S11 and S22 coefficients may be caused by a slight misalignment of the antennas respect to center axis of the chamber. This would influence the way the waves reflect back on the windows and on the walls of the chamber. The S12 and S21 parameters show an increase of the noise and higher attenuation at certain frequency regions of the sweep. The ripples in these measurements are due to the interference (constructive/destructive) of the multiple reflected waves in the windows. The ones also visible without windows are due to the reflections of the walls of the chamber. However, as the influence of the plasma will be studied based on the difference between the signal with and without plasma, these effects will be neglected.

DOI: 10.13009/EUCASS2022-6128

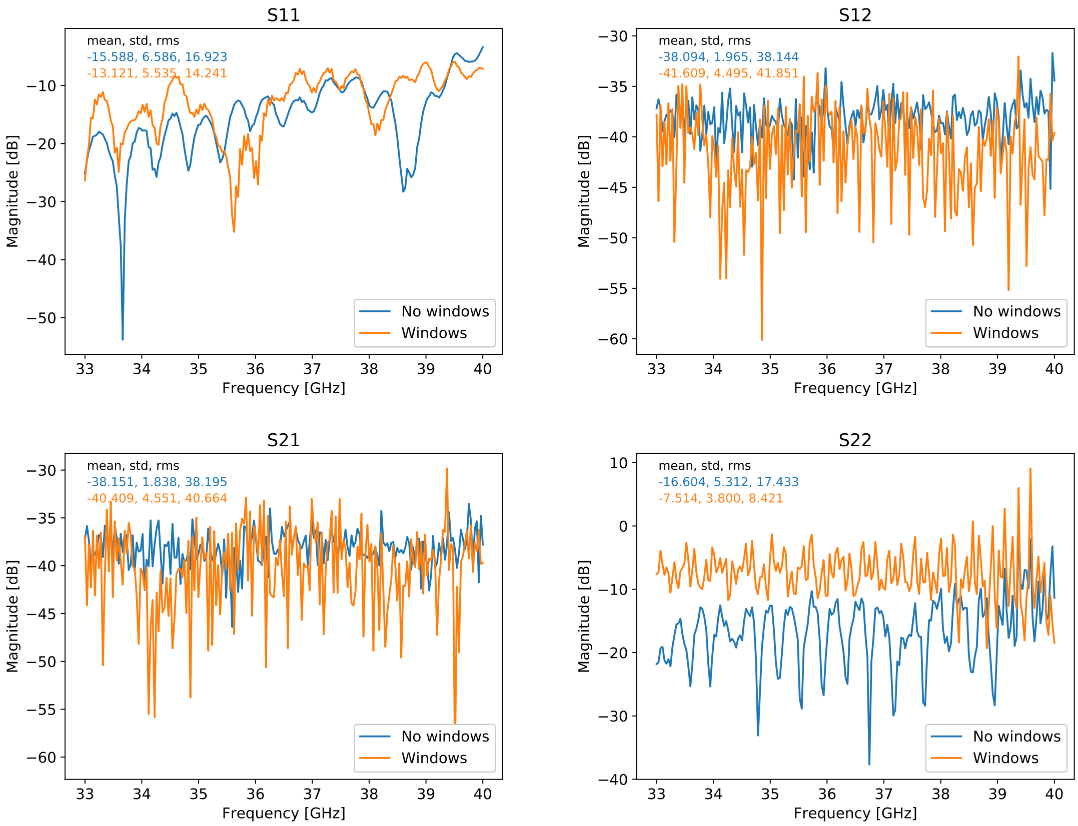

Figure 10: Magnitude of S parameters with and without windows.

4.2.3 Test case: 50 mbar, 320 kW, 40 cm

Figure 11 presents the magnitude of each of the S parameters for a test case at 50 mbar, 320 kW at $d = 40$ cm from the torch exit. The blue lines correspond to the signal without plasma and the orange line with plasma. The magnitude of S11 and S22 remains fairly constant with the average values with and without plasma differing less than 5%. The magnitude of the S12 and S21 parameters over the sweep frequencies range decreases around 10 dB when having the signal propagating through the plasma. Additionally, in these parameters there are certain frequencies at which the signal intensity drops lower than -70 dB, which means that virtually there is no transmission of the signal in that frequency in that instance. The instantaneous differences between S12 and S21 may be related to the operating principle of the VNA and the delay between the acquisition of each of the parameters. This delay may be enough for the state of the plasma to be changed. By analysing five consecutive samples with the background subtracted at the same testing condition (Fig. 12), it is observed that the peaks of highest attenuation are not repeatable at the same signal frequencies. This effect could be caused by the plasma jet fluctuations described in Section 4.2.1, indicating that the thermodynamic state of the plasma might be different at every measurement. The mean value of the magnitude over the whole frequency range (presented alongside the standard deviation and root mean square, respectively, in each of the plots with the same colour as the corresponding sample) shows a variation of less than 3% comparing the different samples. This yields that the overall attenuation and insertion loss for the plasma are fairly constant for each testing condition.

4.2.4 Evolution with power and pressure

40 cm from the torch

As mentioned before, the plasma oscillates at a certain frequency depending on the testing condition. As such, a way of analysing the overall variation of the signal magnitude with power of the Plasmatron and pressure in the chamber while ignoring the jet fluctuations is to plot the mean value of the magnitude of the signal with error bars accounting the standard deviation of the magnitude, as presented in Fig. 13. The condition at 0 kW corresponds to the samples taken with the generator off, hence, without plasma. In this set of measurements, the background is taken in vacuum, with a chamber pressure of around 0.4 mbar. The reflection coefficients are almost constant with power up to

DOI: 10.13009/EUCASS2022-6128

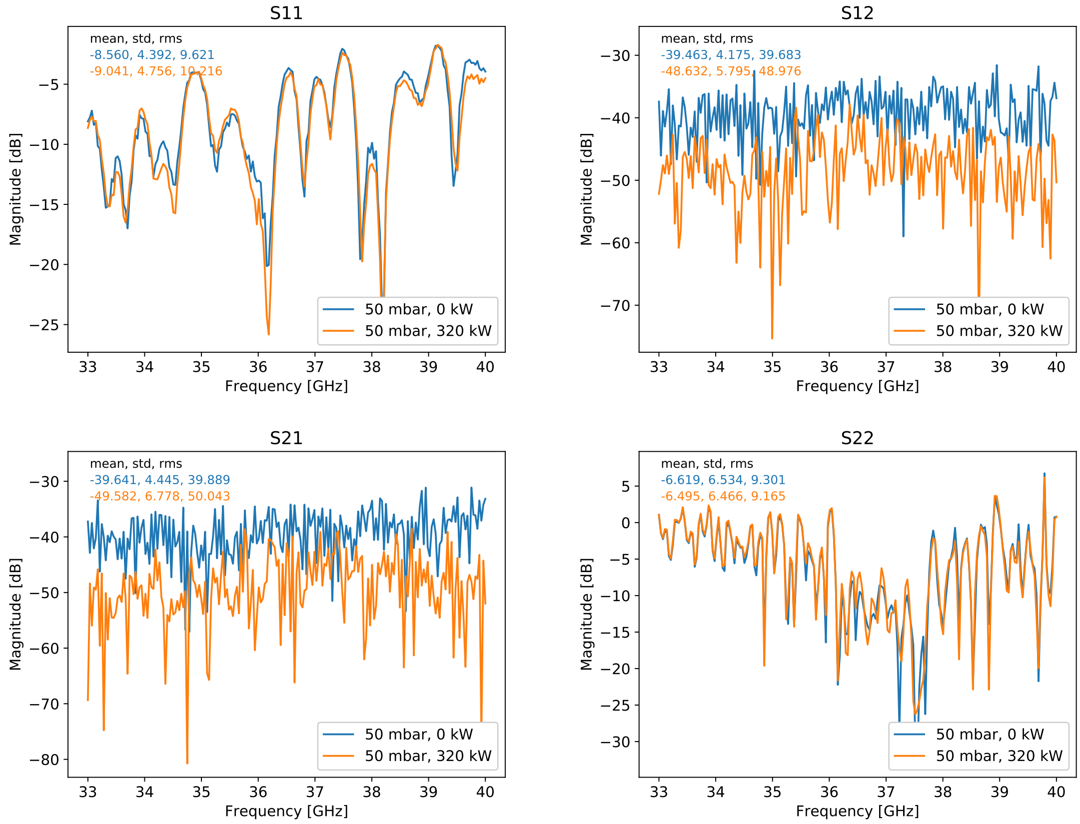

Figure 11: Magnitude of S parameters for 50 mbar, 320 kW at 40 cm from the torch exit.

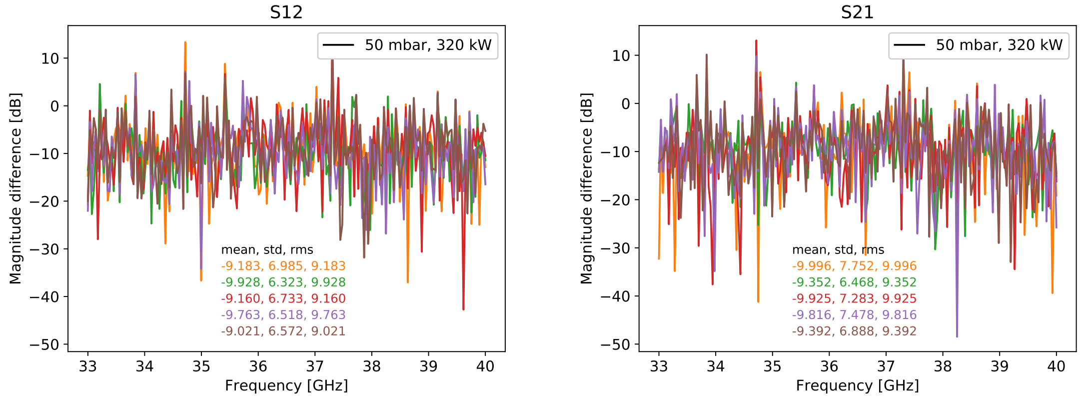

Figure 12: Magnitude difference of the transmission coefficients for 50 mbar, 320 kW at 40 cm for five samples.

320 kW, increasing then slightly up to 600 kW, indicating there are more self reflections occurring at higher pressures. This increase may indicate that the plasma is acting like a wall and more signal is being reflected back to the antennas. The large standard deviations of the coefficients are associated with the ripples caused by the interferences with the windows and the reflections on the wall, as presented in Sec. 4.2.2. Additionally for the transmission coefficients, the signal drops that occur at certain frequencies due to the plasma instabilities also increase the standard deviation of the signal magnitude.

To simplify the presentation of the results, the variation of the mean magnitude of the transmission coefficients is plotted without error bars in Fig. 14 (dots), overlapped with the maximum electron number density (plus symbols and dashed lines). The electron number density distributions are obtained numerically with the COOLFluiD solver (ICP simulations) and the maximum is extracted from the line of sight at 40 cm from the torch exit, for each condition. Comparing the mean magnitude variation and the evolution of the maximum electron density, they follow the same inverted trend (right axis inverted) when increasing power. For the transmission coefficients there is a clear attenuation when increasing power, which then stabilizes above 400 kW. This stabilization is also visible in the numerical simulations. Experimentally, the mean magnitude of the transmission signals increases with the increase from 15 to 50 mbar for low

DOI: 10.13009/EUCASS2022-6128

powers. For powers higher than 320 kW, the mean magnitude is almost independent of the pressure. Assuming local thermochemical equilibrium (LTE), when increasing the pressure, the electron number densities increase. According to this theoretical statement, the attenuation of the signal should also increase when increasing pressure. As the opposite is obtained experimentally, it is concluded that the plasma is not in LTE conditions at 15 mbar.

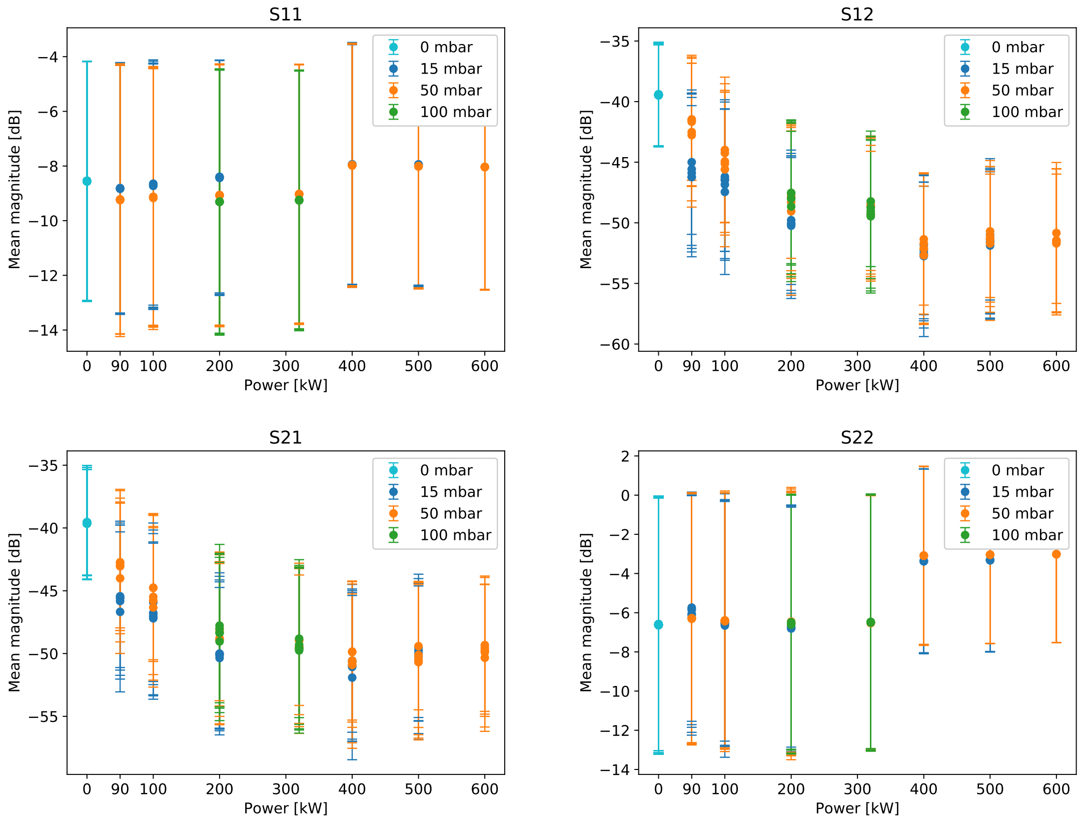

Figure 13: Variation of the mean magnitude with error bars of the S parameters at 40 cm from the torch exit.

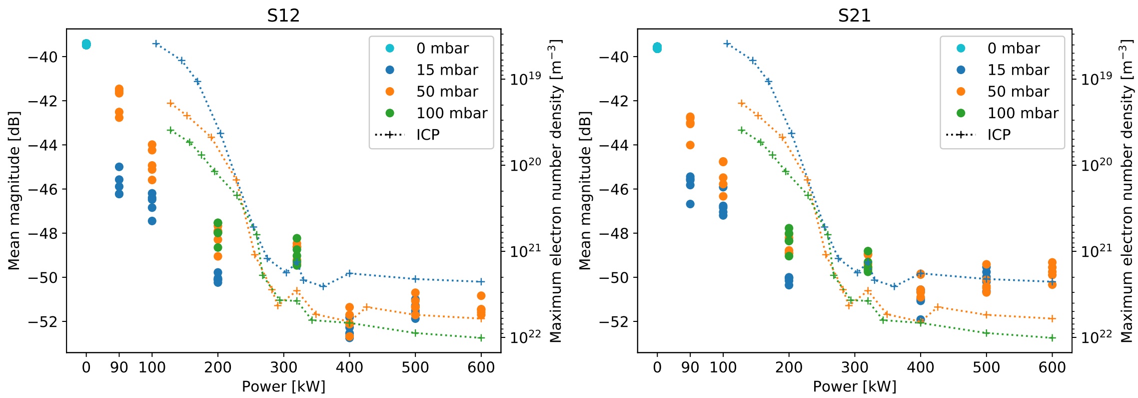

Figure 14: Variation of the mean magnitude of the transmission coefficients and maximum electron number density at 40 cm from the torch exit.

Influence of the distance to the torch

Figure 15 presents the variation of the mean magnitude with the background signal subtracted, ie, the influence of the plasma with the surrounding effects neglected. The circle marker (slightly to the left of the actual power tested) corresponds to the measurements taken at 40 cm from the torch exit, and the cross marker (slightly to the right) corresponds to the measurements at 31 cm from the torch. For the 40 cm case, the background signals are taken in vacuum (and not at the same chamber pressure as during the tests with the plasma), while for the 31 cm case,

DOI: 10.13009/EUCASS2022-6128

the background signals are taken with the chamber at pressures as the one intended for testing. Slight differences are observed in the background signal coefficients when comparing different chamber pressure. Therefore the mean magnitude difference results for 40 cm have an additional small associated error due to the background measurements taken in vacuum. Nevertheless, conclusions for the same pressure can still be retrieved (as they have the same associated error) as well as conclusions on the trends when increasing power.

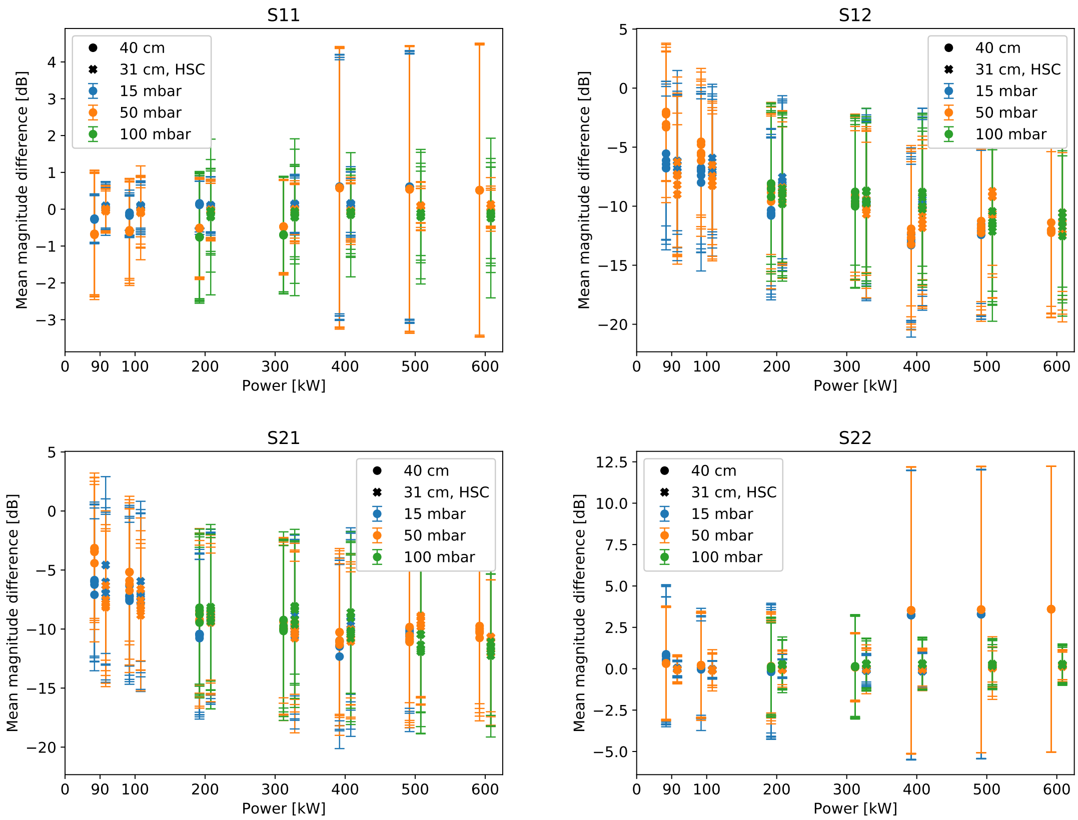

Figure 15: Comparison between the mean magnitude difference of the S parameters at 40 cm and 31 cm from the torch.

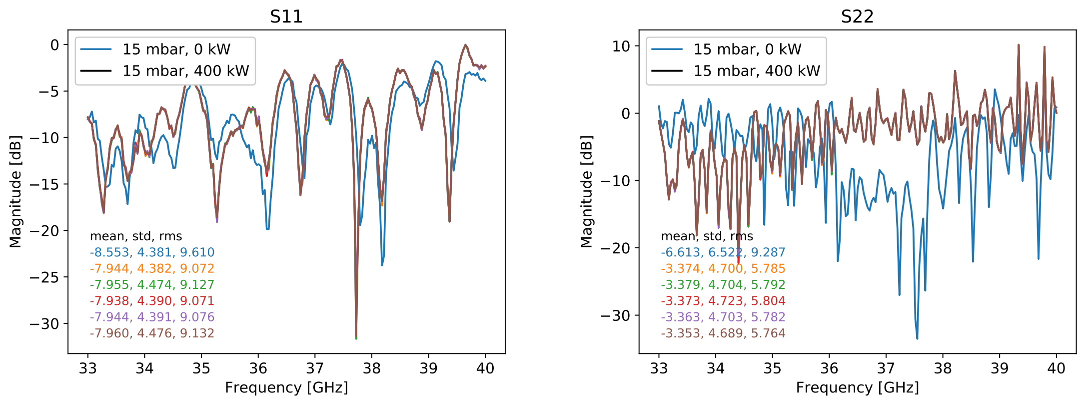

Figure 16: Magnitude of the reflection coefficients for 15 mbar, 400 kW at 40 cm.

For the transmission coefficients, there is a clear decrease of the mean magnitude when increasing the power for both of the positions of the antennas respect to the torch exit. Overall, for the same condition, the attenuation is slightly higher for the antennas at 40 cm. Even though at 31 cm the antennas are closer to the torch and the electron densities are higher (see Fig. 5), the antennas are also closer to the end of the windows and to the chamber wall, and the reflections can be more significant. So a direct comparison cannot be done, but overall the trends are the same when increasing power. When increasing pressure for lower powers, the trend between the two positions is opposite. For 31 cm, the mean magnitude is lower for 50 mbar than for 15 mbar. This may indicate that the flow is also in non equilibrium for 50 mbar at this position of the flow. The reflection coefficients for any condition are very close to

DOI: 10.13009/EUCASS2022-6128

zero with a standard deviation of maximum 3 dB. The only exception occurs for powers from 400 kW at 40 cm from the torch exit. In these cases, the ripples are not occurring at the same frequencies as in the background signal (see Fig. 16). These measurements at high powers for all the pressures have been taken consecutively at the end of the day and the different ripples may be due to a slight movement of the antennas before the acquisition of these conditions, possibly changing the interferences of the signal with the windows and which are not neglected by the background because that was taken at the beginning of the day. This difference is not visible in any the lowest testing powers.

Polarization rotation

The last set of experiments conducted has one antenna (antenna 2) rotated 90^o respect to the other antenna. This way a preliminary study about the polarization rotation due to the plasma can be done. The magnitude of the transmission coefficients, without plasma, intrinsically decreases around 10 dB due to the linear polarization of the antennas. Figure 17 presents the variation of the mean magnitude with power and pressure without background signal for the cases when the electric field of both antennas is aligned (circle marker, slightly to the left of the tested power) and for when it is perpendicular (cross marker, slightly to the right). In both cases the antennas are 31 cm from the torch exit. When turning on the plasma, the signal magnitude still decreases, indicating that the initial electric field of the antennas is not completely perpendicular to each other and there is still attenuation affecting the signal. Comparing the transmission coefficients, the slope for the decrease in the magnitude for each of the coefficients is almost the same. At 15 mbar, and 90 and 100 kW the difference is slightly higher than 0 dB when the electric fields are perpendicular. A higher than 0 dB means that the magnitude of signal received with the plasma is stronger than the magnitude of the signal without plasma. These results have a high uncertainty, but the positive magnitude difference indicates a Faraday rotation caused by the plasma. Further tests will be conducted to confirm and to study the Faraday rotation caused by the plasma.

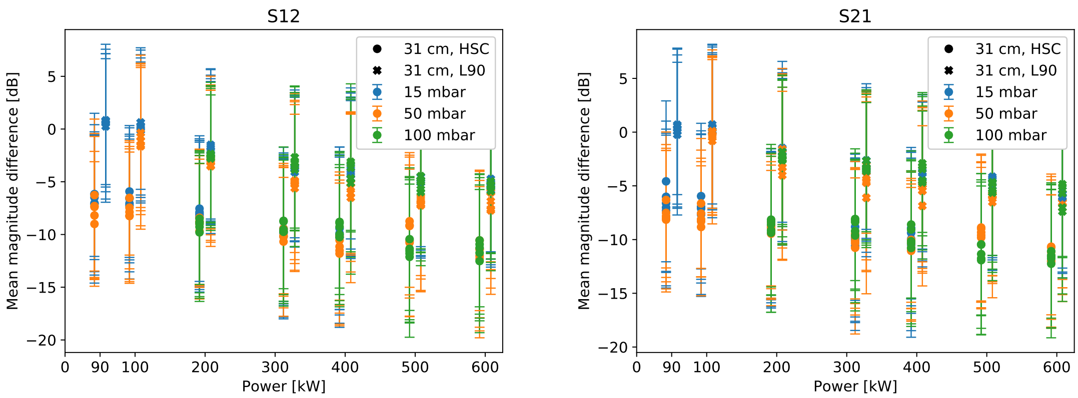

Figure 17: Comparison between the mean magnitude difference of the transmission coefficients for 0^o (label: *31 cm, HSC*) and 90^o (label: *31 cm, L90*) between the electric fields of each antenna.

5. Conclusions and future work

Radio signal propagation in an air plasma flow has been studied for a combination of static pressures and power settings. The tests have been conducted by placing two antennas across the plasma jet at the VKI-Plasmatron facility, and by measuring their signals with a vector network analyser. Additionally, high speed imaging has allowed to characterize the unsteadiness of the plasma jet.

The imagining analysis has shown significant jet fluctuations. The brightest light emission has been found to be located along the axis and closer to the torch exit, while further from the exit the fluctuations seem to be more unstable. Nevertheless, there is a main frequency component of the fluctuations, which is dependent on the testing conditions. This frequency is increasing with power and decreasing with chamber pressure. An exception has been verified for the highest power and further tests with longer acquisition times of the high speed camera are suggested to be performed to verify this result.

The radio signal propagation has been studied initially without plasma to verify the effect of the windows and of the chamber walls. Clear ripples have been observed due to these interferences. To reduce the amount of reflections on the chamber walls, tests with more directive antennas are suggested. To minimize these effects in this work, the effect of the plasma has been studied based on the difference between the signal with and without plasma. As the state

DOI: 10.13009/EUCASS2022-6128

of the plasma is changing during one single VNA measurement, a direct comparison between each sample cannot be performed. To improve these results, phase lock measurements are suggested to average the results for each frequency at the exact same plasma condition. To neglect the influence of the plasma unsteadiness, the signal has been averaged over the frequency sweep range. Clear attenuations of the signal have been verified, ranging between 5 and 15 dB depending on the testing conditions. The evolution of the variation of the mean magnitude in function of power has been found to follow the inverse trend of the numerical electron number densities, as expected. No significant changes with pressure have been verified for high powers. Additional tests are planned to measure electron number densities in the Plasmatron facility using emission spectroscopy, by measuring the Stark broadening of the H_β line, and using a Langmuir probe for comparison with the experimental results presented in this work. Further tests are also suggested to study the group delay and Faraday rotation of the signal due to the plasma.

6. Acknowledgments

Diana Luís research is funded by a doctoral fellowship (2021.04930.BD) granted by Fundação para a Ciência e Tecnologia (FCT Portugal). The MEESST project is funded by the European Union's Horizon 2020 research and innovation programme under grant agreement No 899298.

References

[1] M. Keidar, M. Kim, and I. Boyd. Electromagnetic Reduction of Plasma Density During Atmospheric Reentry and Hypersonic Flights. *Journal of Spacecraft and Rockets*, 45(3):455–453, 2008. https://doi.org/10.2514/1.32147.

[2] D. D. Morabito. The spacecraft communications blackout problem encountered during passage or entry of planetary atmospheres. Technical report progress report 42-150, IPN NASA Jet Propulsion Laboratory, 2002.

[3] W. L. Grantham. Flight results of a 25 000-foot-persecond reentry experiment using microwave reflectometers to measure plasma electron density and standoff distances. Technical report technical note d-6062, NASA Langley Research Center, 1970.

[4] R. Lehnert and B. Rosenbaum. Plasma Effects on Apollo Re-entry Communication. Technical Report TN D-2732, NASA, 1965.

[5] M. G. Dunn. Comparison between predicted and measured blackout boundaries for earth entry of Apollo. *NASA Spec. Publ.*, 252(33), 1971.

[6] P. W. Huber. Deduction of reentry plasma properties about manned orbital spacecraft from radio signal attenuation data. Technical report, NASA Langley Research Center, 1967.

[7] R. P. Starkey. Hypersonic Vehicle Telemetry Blackout Analysis. *Journal of Spacecrafts and Rockets*, 52(2), 2015. https://doi.org/10.2514/1.A32051.

[8] R. P. Starkey, M. J. Lewis, and C. H. Jones. Active Flowfield Modification for Plasma Telemetry. In *International Test and Evaluation Association Conference ITEA*, April 2002.

[9] J. Cheng, K. Jin, Y. Kou, R. Hu, and X. Zheng. An electromagnetic method for removing the communication blackout with a space vehicle upon re-entry into the atmosphere. *Journal of Applied Physics*, 121, 2017. https://doi.org/10.1063/1.4976213.

[10] J. P. Rybak and R. J. Churchill. Progress in Reentry Communications. *IEEE Transactions on Aerospace and Electronic Systems*, AES-7(5):879–894, 1971. https://doi.org/10.1109/TAES.1971.310328.

[11] C. Jones. Report from the Workshop on Communications Through Plasma During Hypersonic Flight. page 25, August 2006. https://doi.org/10.2514/6.2009-1718.

[12] E. Gillman, J. Foster, and I. Blankson. Review of Leading Approaches for Mitigating Hypersonic Vehicle Communications Blackout and a Method of Ceramic Particulate Injection Via Cathode Spot Arcs for Blackout Mitigation. Technical Report NASA/TM - 2010-216220, NASA, 2010.

[13] I. F. Belov, V. Y. Borovoy, V. A. Gorelov, A. Y. Kireev, A. S. Korolev, and E. A. Stepanov. Investigation of Remote Antenna Assembly for Radio Communication with Reentry Vehicle. *Journal of Spacecraft and Rockets*, 38(2):249–256, 2001. https://doi.org/10.2514/2.3678.

DOI: 10.13009/EUCASS2022-6128

[14] R. Savino, D. Paterna, M. De Stefano Fumo, and M. D'Eli. Plasma-Radiofrequency Interactions Around Atmospheric Re-Entry Vehicles: Modelling and Arc-Jet Simulation. *The Open Aerospace Engineering Journal*, 3:76–85, 11 2010. `https://doi.org/10.2174/1874146001003010076`.

[15] S. A. Bendoukha, K. Okuyama, B. Szasz, and S. Takayuki. Experimental Method Using Arc Wind Tunnel to Simulate A New Technique For Communicating With A Reentry Probe Having A Thermal Shield Made Of LATS Materials. *International Journal of Research*, 5:1–12, 2017. `https://10.5281/zenodo.345434`.

[16] K. Lemmer, A. Gallimore, and T. Smith. Experimental Results for Communications Blackout Amelioration Using Crossed Electric and Magnetic Fields. *Journal of Spacecraft and Rockets*, November-December 2009.

[17] S. I. Schlachter, J. Brand, H. Fillinger, W. Goldacker, A. Kling, B. Ringsdorf, U. Walschburger, J. Willms, H. Wu, A. Gülhan, L. Steffens, Y. A. Kurakin, and S. A. Poniaev. Performance of conduction-cooled HTS Magnet in radio blackout mitigation experiment. IWC-HTS, 2017.

[18] H. Hodara. The Use of Magnetic Fields in the Elimination of the Re-Entry Radio Blackout. *Proceedings of the IRE*, 49:1825–1830, 1962. `https://10.1109/JRPROC.1961.287709`.

[19] R. Starkey, R. Lewis, and C. Jones. Plasma Telemetry in Hypersonic Flight. *International Telemetering Conference, International Foundation for Telemetering*, (Paper 02-15-2), 2002.

[20] R. Starkey, R. Lewis, and C. Jones. Electromagnetic Wave/ Magnetoactive Plasma Sheath Interaction for Hypersonic Vehicle Telemetry Blackout Analysis. *34th AIAA Plasmadynamics and Lasers Conference*, (AIAA Paper 2003-4167), 2003.

[21] J. G. Proakis and M. Salehi. *Fundamentals of Communication Systems*. Pearson, 2014. ISBN: 9780133354850.

[22] S. Victor Hum. Ionospheric propagation. Radio and Microwave Wireless Systems, University of Toronto.

[23] K. U. Ingard. *Fundamentals of Waves and Oscillations*. Cambridge University Press, July 1988. ISBN: 9780521339575.

[24] F. Caspers. RF engineering basic concepts: S-parameters. *CERN Yellow Report*, (CERN-2011-007):67–93, 2011. `https://doi.org/10.48550/arXiv.1201.2346`,.

[25] B. Bottin, O. Chazot, M. Carbonaro, V. Van Der Haegen, and S. Paris. The VKI Plasmatron Characteristics and Performance. *Measurement Techniques for High Enthalpy and Plasma Flows*, April 2000.

[26] B. Bottin. *Aerothermodynamic Model of an Inductively-Coupled Plasma Wind Tunnel: Numerical and Experimental Determination of the Facility Performance*. PhD thesis, von Karman Institue for Fluid Dynamics, 1999.

[27] G. Degrez, D. Vanden Abeele, P. Barbante, and B. Bottin. Numerical Simulation of Inductively Coupled Plasma Flows under Chemical Non-equilibrium. *International Journal of Numerical Methods for Heat & Fluid Flow*, 14(4):538–558, 2004. `https://doi.org/10.1108/09615530410532286`.

[28] D. Vanden Abeele and G. Degrez. Efficient computational model for inductive plasmas flows. *AIAA Journal*, 38(2):234–242, 2000. `https://doi.org/10.2514/2.977`.

[29] A. Lani. *An Object Oriented and High Performance Platform for Aerothermodynamics Simulation*. PhD thesis, 2009.

[30] M. J. B. Scoggins. *Development of numerical methods and study of coupled flow, radiation, and ablation phenomena for atmospheric entry*. PhD thesis, von Karman Institute for Fluid Dynamics and CentraleSupÃ©lec, 2017.

[31] A. Viladegut. *Assessment of Gas-Surface Interaction Modelling for Lifting Body Re-Entry Flight Design*. PhD thesis, von Karman Institute for Fluid Dynamics and Universitàt Politècnica de Catalunya, 2017.

[32] Understanding VNA Calibration. Technical report, Anritsu Company, 2012. `http://anlage.umd.edu/Anritsu_understanding-vna-calibration.pdf`, last accessed 06 May 2022.

[33] A. Fagnani, D. Le Quang Huy, B. Helber, S. Demange ans A. Turchi, O. Chazot, and A. Hubin. Investigation of a Free-Stream Air Plasma Flow by Optical Emission Spectroscopy and Comparison to Magnetohydrodynamics Simulations. In *AIAA SciTech Forum*, January 2020.

DOI: 10.13009/EUCASS2022-6128

[34] A. Cipullo, B. Helber, F. Panerai, L. Zeni, and O. Chazot. Investigation of Freestream Plasma Flow Produced by Inductively Coupled Plasma Wind Tunnel. *Journal of Thermophysics and Heat Transfer*, 28(3), July-September 2014.